

Functional renormalization group for classical liquids without recourse to hard-core reference systems: A study of three-dimensional Lennard-Jones liquids

Takeru Yokota,^{1, 2, *} Jun Haruyama,^{3, †} and Osamu Sugino^{4, ‡}

¹Faculty of Engineering, Osaka Institute of Technology, Asahi-ku, Osaka, 535-8585, Japan

²RIKEN Center for Interdisciplinary Theoretical and Mathematical Sciences (iTHEMS), Wako, 351-0198, Japan

³RIKEN Pioneering Research Institute (PRI), Wako, 351-0198, Japan

⁴Institute for Solid State Physics, The University of Tokyo, Kashiwa, Chiba 277-8581, Japan

(Dated: October 21, 2025)

In our previous work [Phys. Rev. E **104**, 014124 (2021)], we developed a method for analyzing classical liquids using the functional renormalization group (FRG) without relying on a hard-core reference system. In this paper, we extend that method to three-dimensional liquids. We describe an efficient approach for performing the spatial integrals that appear in the renormalization group equations, which is essential for realizing numerical calculations in three dimensions. As a demonstration of our method, we present its application to the Lennard-Jones liquid. By calculating thermodynamic quantities and the pair distribution function near the critical point, we find that, compared with integral equation methods, the FRG approach preserves thermodynamic consistency much more effectively and more accurately reproduces the results of molecular dynamics simulations. Moreover, we successfully capture characteristic phase-transition phenomena with FRG, such as the softening of pressure near the critical temperature. Our results suggest that FRG can provide a more accurate framework for describing classical liquids than conventional methods such as integral equation theories.

I. INTRODUCTION

The development of analytical methods for classical liquids has long been a central challenge in statistical mechanics [1]. In recent years, advances in simulation techniques like molecular dynamics (MD) and Monte Carlo (MC) methods have made it possible to investigate the microscopic state of liquids directly from fundamental principles. However, obtaining highly accurate results still requires substantial computational cost, making it difficult to address slow or large-scale phenomena such as phase transitions. Therefore, the importance of liquid theory remains undiminished, serving as a theoretical framework for systematically understanding the mechanisms behind physical phenomena with a small number of parameters and for rapidly predicting physical properties. The role of liquid theory is not limited to understanding the properties of liquids themselves. For example, it has also evolved into a practical method for efficiently incorporating solvent effects into electronic structure calculations [2]. This method enables the uniform treatment of the distribution of electrons and nuclei (particles) under a single density-based principle.

However, even the theoretical framework for simple liquids is still incomplete. Many integral equation approaches such as the hypernetted chain and Percus-Yevick equation have a mean-field character, and their predictive accuracy depends heavily on the precision of the approximation known as the closure relation [3–

6]. In addition, such approaches tend to exhibit significant thermodynamic inconsistency—that is, discrepancies arising when the same quantity is computed using different thermodynamic relations [1]. Attempts to improve predictive power by imposing physical self-consistency (e.g., MHNC [7], RY [8]) have achieved some success but have not led to a universal solution. This is also the case in the field of classical density functional theory (cDFT) [9–12]. For repulsive interactions, such as those in hard-sphere systems, fundamental measure theory (FMT) [13–16] has enabled highly accurate descriptions. However, it is still an issue to incorporate attractive interactions essential for real liquids beyond a perturbative treatment [17]. Thus, establishing a general-purpose liquid theory that is both efficient under all conditions and has an accuracy comparable to MD simulations remains an important and ongoing challenge in condensed matter physics.

Here, we focus on the renormalization group as an alternative approach to describing liquids [18–30]. This method has been developed primarily as a framework for treating critical phenomena in liquids. Among such approaches, the well-known hierarchical reference theory (HRT) [18, 20, 22, 25, 26, 28] takes a system with hard-core repulsion as the reference system and gradually incorporates the effects of the attractive part of the intermolecular interactions, starting from short-range components. This procedure is formulated in terms of differential equations (flow equations), and solving them allows one to analyze the properties of the critical point. Since apparent divergences arise when handling hard-core repulsion within the flow equations, the renormalization group is typically applied only to the attractive part. However, this approach requires prior knowledge of hard-core systems and does not provide a fully consistent anal-

* takeru.yokota@oit.ac.jp

† jun.haruyama@riken.jp

‡ sugino@issp.u-tokyo.ac.jp

ysis based on the flow equations. Moreover, while the renormalization group method should in principle be applicable to liquids beyond just the critical point, studies in this broader context are relatively scarce compared to those focused on critical phenomena.

Against this backdrop, in our previous work [31] we developed a flow-equation-based method for calculating liquid structures without relying on a hard-core reference system and applicable beyond the critical point. Our approach is grounded in the functional renormalization group (FRG), a formulation based on functionals with a rigorous theoretical foundation. Originally introduced in quantum field theory [32–35] and later applied in the context of quantum systems to density functional theory [36–47], we adapted this framework to construct renormalization group equations for classical systems. From these equations, we derived hierarchical flow equations for multiparticle distribution functions. By reformulating them in terms of cavity distribution functions, we discovered that the apparent divergences arising from hard-core interactions could be eliminated. In that earlier study, we applied the method to an exactly solvable one-dimensional system, where it was suggested that FRG offers better accuracy in the high-density regime compared to integral equation methods.

In this paper, we extend our previous work [31] to apply FRG to three-dimensional liquids. As in the earlier study, we introduce a functional flow equation associated with the evolution of the pair interaction. From this, we derive hierarchical flow equations for the cavity distribution functions, which we solve by truncating them using the Kirkwood superposition approximation (KSA) [48]. A key step in realizing the application of this method to three-dimensional systems is the efficient evaluation of the spatial integrals appearing in the flow equations. To this end, we introduce a method based on Legendre polynomial expansion [49] to compute these integrals efficiently. Furthermore, we consider the evolution with respect to the interaction range so as to further reduce the dimensionality of the integrals.

In the latter part of this paper, we apply our method to the Lennard-Jones liquid. Here, we test the performance of our approach near the liquid–gas critical point exhibited by this model. We first compute thermodynamic quantities such as pressure, as well as the pair distribution function, at temperatures above the critical point, and assess the accuracy by comparing the results with MD and integral equation methods. As the density increases, integral equation methods exhibit a significant loss of thermodynamic consistency and produce results that deviate from MD simulations. Even in such cases, however, the FRG approach maintains thermodynamic consistency much more effectively and tends to reproduce the MD results with higher accuracy. We also perform calculations near the critical temperature. By plotting pressure as a function of density, we reproduce the softening of pressure as the system approaches the critical temperature. Furthermore, below the critical tempera-

ture, our method remains applicable in the stable and metastable regions, while in the spinodal region the bulk modulus approaches zero during the flow, causing the calculation to break down, consistent with the expected behavior.

This paper is organized as follows: In Sec. II, we present the formulation of our method and introduce an efficient approach for evaluating the three-dimensional spatial integrals appearing in the flow equations. In Sec. III, we describe the application of our method to the Lennard-Jones liquid. Section IV is devoted to the conclusion.

II. FORMALISM AND TECHNICS

We introduce our method for analyzing three-dimensional classical liquids. First, we review the approaches presented in our previous work [31] in Secs. II A and II B. We then describe in Sec. II C the method developed to extend the analysis to the three-dimensional case.

A. Flow equations for hard-core systems

1. Functional flow equation

We consider a classical particle system interacting via a two-body potential $v_\lambda(\mathbf{r} - \mathbf{r}')$, where $\mathbf{r} - \mathbf{r}'$ is the distance between two particles, under an external field $U(\mathbf{r})$. Here, a flow parameter $\lambda \in [0, 1]$ is introduced into the two-body interaction. We study the evolution equation with respect to λ , assuming that $v_\lambda(\mathbf{r} - \mathbf{r}')$ interpolates between a reference system, $v_0(\mathbf{r} - \mathbf{r}') = v_{\text{ref}}(\mathbf{r} - \mathbf{r}')$, and the target system of interest, $v_1(\mathbf{r} - \mathbf{r}') = v(\mathbf{r} - \mathbf{r}')$. In the spirit of the renormalization group, the evolution of $v_\lambda(\mathbf{r} - \mathbf{r}')$ is arranged so that the short-range components of $v(\mathbf{r} - \mathbf{r}') - v_{\text{ref}}(\mathbf{r} - \mathbf{r}')$ are incorporated first, followed gradually by the long-range components.

We adopt the grand canonical distribution and define the free energy density functional $F_\lambda[\rho]$, where $\rho(\mathbf{r})$ denotes the expectation value of the particle number density in this distribution, hereafter simply referred to as the density. By determining $F_\lambda[\rho]$, we not only obtain the thermodynamic quantities of the system but also, through its derivatives, the direct correlation functions, thereby gaining access to all information on particle correlations. To define $F_\lambda[\rho]$, we first introduce the grand partition function $\Xi_\lambda[\bar{\psi}]$ under inverse temperature β and chemical potential μ :

$$\Xi_\lambda[\bar{\psi}] := \sum_{N=0}^{\infty} \int d\mathbf{r}_1 \cdots \int d\mathbf{r}_N \frac{e^{-\sum_{i < j}^N \bar{v}_\lambda(\mathbf{r}_i - \mathbf{r}_j) + \sum_{i=1}^N \bar{\psi}(\mathbf{r}_i)}}{\Lambda^{3N} N!}. \quad (1)$$

Here, Λ is the thermal de Broglie wavelength, $\bar{v}_\lambda(\mathbf{r}_i - \mathbf{r}_j) = \beta v_\lambda(\mathbf{r}_i - \mathbf{r}_j)$ is the dimensionless two-body in-

teraction, and $\bar{\psi}(\mathbf{r}) = \beta(\mu - U(\mathbf{r}))$ is the dimensionless intrinsic chemical potential. The functional $F_\lambda[\rho]$ is the Legendre transform of the thermodynamic potential $\Omega_\lambda[\bar{\psi}] = -\frac{1}{\beta} \ln \Xi_\lambda[\bar{\psi}]$. For notational simplicity, we introduce the dimensionless free energy density functional $\bar{F}_\lambda[\rho] = \beta F_\lambda[\rho]$ and the dimensionless thermodynamic potential $\bar{\Omega}_\lambda[\bar{\psi}] = \beta \Omega_\lambda[\bar{\psi}]$. The definition of $\bar{F}_\lambda[\rho]$ is given by

$$\bar{F}_\lambda[\rho] = \int d\mathbf{r} \rho(\mathbf{r}) \bar{\psi}_\lambda[\rho](\mathbf{r}) + \bar{\Omega}_\lambda[\bar{\psi}_\lambda[\rho]]. \quad (2)$$

Here, $\bar{\psi}_\lambda[\rho](\mathbf{r})$ is the function $\bar{\psi}(\mathbf{r})$ that maximizes the right-hand side, and therefore satisfies the following condition.

$$\rho(\mathbf{r}) = -\frac{\delta \bar{\Omega}_\lambda[\bar{\psi}_\lambda[\rho]]}{\delta \bar{\psi}(\mathbf{r})}. \quad (3)$$

Since the derivative of $-\bar{\Omega}_\lambda[\bar{\psi}]$ gives the expected value of the density, it follows that $\bar{\psi}_\lambda[\rho](\mathbf{r})$ is the intrinsic chemical potential required to realize the density $\rho(\mathbf{r})$.

The FRG equation of $\bar{F}_\lambda[\rho]$ with respect to λ is known to be expressible in a closed form as follows [18, 31]:

$$\begin{aligned} & \partial_\lambda \bar{F}_\lambda[\rho] \\ &= \frac{1}{2} \int d\mathbf{r} \int d\mathbf{r}' \partial_\lambda \bar{v}_\lambda(\mathbf{r} - \mathbf{r}') \\ & \quad \times \left(\rho(\mathbf{r})\rho(\mathbf{r}') + \left(\frac{\delta^2 \bar{F}_\lambda[\rho]}{\delta \rho \delta \rho} \right)^{-1}(\mathbf{r}, \mathbf{r}') - \rho(\mathbf{r})\delta(\mathbf{r} - \mathbf{r}') \right). \end{aligned} \quad (4)$$

This equation alone determines $F_\lambda[\rho]$ exactly. However, a numerical method for solving such a functional differential equation has not been established, and in practice, some form of approximation is necessary. A mainstream approach involves applying a functional Taylor expansion to the functional differential equation to derive a hierarchy of equations for the expansion coefficients. This hierarchy is then truncated and solved. In fact, such methods have been developed in the context of FRG [50]. This approach provides a non-perturbative framework that does not rely on the weakness of the interaction.

To solve the evolution equation (4), prior knowledge of the initial reference system is required. The simplest choice for the reference system is the non-interacting case $v_{\text{ref}} = 0$, for which $\Omega_\lambda[\bar{\psi}]$ can be expressed analytically:

$$\bar{F}_0[\rho] = \int d\mathbf{r} \rho(\mathbf{r}) (\ln(\Lambda^3 \rho(\mathbf{r})) - 1). \quad (5)$$

The problem arises when v_λ interpolates between a non-interacting reference system and a system with hard-core repulsion: the interaction flow $\partial_\lambda v_\lambda$ becomes divergent at

short distances, leading to numerical instability. In practice, classical liquid analysis based on flow equations—such as in the HRT—typically treats the hard-core part as the reference system and applies the flow equation only to the long-range attractive part. This kind of approach requires prior knowledge of the hard-core system and prevents computation within a fully self-consistent framework based entirely on the flow equation.

However, this divergence is only apparent, and in approaches based on functional Taylor expansion, the issue can be avoided by reformulating the hierarchy of equations. Specifically, by rewriting the system in terms of a hierarchy for the cavity distribution function, the divergence can be circumvented. This is one of the main results of our previous work [31].

2. Hierarchical equations for cavity distribution functions

To define the cavity distribution functions, we first introduce the n -particle distribution function:

$$g_\lambda^{(n)}(\mathbf{r}_1, \dots, \mathbf{r}_n) = \frac{\rho_\lambda^{(n)}(\mathbf{r}_1, \dots, \mathbf{r}_n)}{\rho(\mathbf{r}_1) \dots \rho(\mathbf{r}_n)}, \quad (6)$$

where the n -particle density $\rho_\lambda^{(n)}(\mathbf{r}_1, \dots, \mathbf{r}_n)$ is given by the following functional derivative expression:

$$\rho_\lambda^{(n)}(\mathbf{r}_1, \dots, \mathbf{r}_n) = \frac{e^{\bar{\psi}_\lambda[\rho](\mathbf{r}_1)} \dots e^{\bar{\psi}_\lambda[\rho](\mathbf{r}_n)}}{\Xi_\lambda[\bar{\psi}_\lambda[\rho]]} \frac{\delta^n \Xi_\lambda[\bar{\psi}_\lambda[\rho]]}{\delta e^{\bar{\psi}(\mathbf{r}_1)} \dots \delta e^{\bar{\psi}(\mathbf{r}_n)}}. \quad (7)$$

The n -particle cavity distribution function $y_\lambda^{(n)}(\mathbf{r}_1, \dots, \mathbf{r}_n)$ is defined in terms of $g_\lambda^{(n)}(\mathbf{r}_1, \dots, \mathbf{r}_n)$ as follows:

$$y_\lambda^{(n)}(\mathbf{r}_1, \dots, \mathbf{r}_n) = e^{\sum_{i < j} \bar{v}_\lambda(\mathbf{r}_i - \mathbf{r}_j)} g_\lambda^{(n)}(\mathbf{r}_1, \dots, \mathbf{r}_n). \quad (8)$$

Due to this exponential factor, the direct interaction among the n particles is effectively suppressed, and it is known that $y_\lambda^{(n)}(\mathbf{r}_1, \dots, \mathbf{r}_n)$ remains a continuous function even in the presence of divergent repulsions or discontinuities in the interaction potential [1].

Through Eq. (2) and Eqs. (6)-(8), $y_\lambda^{(n)}(\mathbf{r}_1, \dots, \mathbf{r}_n)$ is found to be related to the n th functional derivative of $\bar{F}_\lambda[\rho]$. Therefore, by differentiating the flow equation (4) n times, one can derive a corresponding flow equation for $y_\lambda^{(n)}(\mathbf{r}_1, \dots, \mathbf{r}_n)$. Here, we consider the case of uniform density $\rho(\mathbf{r}) = \rho$, which is typically of interest in liquid state theory. In this case, translational symmetry implies that $y_\lambda^{(n)}(\mathbf{r}_1, \dots, \mathbf{r}_n)$ depends only on the relative positions $\mathbf{r}_1 - \mathbf{r}_n, \dots, \mathbf{r}_{n-1} - \mathbf{r}_n$. Without loss of generality, we may set $\mathbf{r}_n = \mathbf{0}$ and write $y_\lambda^{(n)}(\mathbf{r}_1, \dots, \mathbf{r}_{n-1})$. In addition, $\bar{\psi}_\lambda(\mathbf{r})$ becomes spatially uniform and is denoted by a constant $\bar{\psi}_\lambda$. As derived in Ref. [31], differentiating Eq. (4) yields the following flow equation:

$$\partial_\lambda \frac{\bar{F}_\lambda}{N} = -\frac{\rho}{2} \int d\mathbf{r} \partial_\lambda [e^{-\bar{v}_\lambda(\mathbf{r})}] y_\lambda^{(2)}(\mathbf{r}), \quad (9)$$

$$\partial_\lambda \bar{\psi}_\lambda = -\beta K_{T,\lambda} \int d\mathbf{r} \partial_\lambda [e^{-\bar{v}_\lambda(\mathbf{r})}] y_\lambda^{(2)}(\mathbf{r}) \left(1 + \frac{\rho}{2} \int d\mathbf{r}' \left[e^{-\bar{v}_\lambda(\mathbf{r}+\mathbf{r}')-\bar{v}_\lambda(\mathbf{r}')} \frac{y_\lambda^{(3)}(\mathbf{r}+\mathbf{r}', \mathbf{r}')}{y_\lambda^{(2)}(\mathbf{r})} - 1 \right] \right), \quad (10)$$

$$\begin{aligned} & \partial_\lambda \ln y_\lambda^{(n)}(\mathbf{r}_1, \dots, \mathbf{r}_{n-1}) \\ &= \partial_\lambda \bar{\psi}_\lambda \left(n + \rho \int d\mathbf{r} \left[e^{-\sum_{i=1}^n \bar{v}_\lambda(\mathbf{r}_i - \mathbf{r})} \frac{y_\lambda^{(n+1)}(\mathbf{r}_1, \dots, \mathbf{r}_{n-1}, \mathbf{r})}{y_\lambda^{(n)}(\mathbf{r}_1, \dots, \mathbf{r}_{n-1})} - 1 \right] \right) + \rho \int d\mathbf{r} \partial_\lambda [e^{-\sum_{i=1}^n \bar{v}_\lambda(\mathbf{r}_i - \mathbf{r})}] \frac{y_\lambda^{(n+1)}(\mathbf{r}, \mathbf{r}_1, \dots, \mathbf{r}_{n-1})}{y_\lambda^{(n)}(\mathbf{r}_1, \dots, \mathbf{r}_{n-1})} \\ &+ \frac{\rho^2}{2} \int d\mathbf{r} \int d\mathbf{r}' \partial_\lambda [e^{-\bar{v}_\lambda(\mathbf{r} - \mathbf{r}')} y_\lambda^{(2)}(\mathbf{r} - \mathbf{r}')] \left[e^{-\sum_{i=1}^n \bar{v}_\lambda(\mathbf{r}_i - \mathbf{r}) - \sum_{i=1}^n \bar{v}_\lambda(\mathbf{r}_i - \mathbf{r}')} \frac{y_\lambda^{(n+2)}(\mathbf{r}, \mathbf{r}', \mathbf{r}_1, \dots, \mathbf{r}_{n-1})}{y_\lambda^{(2)}(\mathbf{r} - \mathbf{r}') y_\lambda^{(n)}(\mathbf{r}_1, \dots, \mathbf{r}_{n-1})} - 1 \right], \quad (11) \end{aligned}$$

where $N = \rho \int d\mathbf{r}$ is the particle number and

$$K_{T,\lambda} = \frac{\rho}{\beta} \left[1 + \rho \int d\mathbf{r} (g_\lambda^{(2)}(\mathbf{r}) - 1) \right]^{-1} \quad (12)$$

is the isothermal bulk modulus. Note that $\mathbf{r}_n = \mathbf{0}$ in Eq. (11). The first-, second-, and third equations correspond to the zeroth, first, and n th ($n \geq 2$) functional derivatives of Eq. (4), respectively. In all of these equations, $\bar{v}_\lambda(\mathbf{r})$ appears exclusively inside exponential functions. As a result, even if $\bar{v}_\lambda(\mathbf{r})$ includes divergent repulsive interactions, such divergences do not manifest in the flow equations themselves. Thanks to this, by setting $\bar{v}_0(\mathbf{r}) = 0$ we can use the non-interacting case as the initial condition and incorporate the effects of the divergent repulsion by solving the flow equations without encountering apparent divergences. In this case, the initial condition is $y_0^{(n)}(\mathbf{r}_1, \dots, \mathbf{r}_{n-1}) = 1$, and the dimensionless excess free energy per particle \bar{F}^{ex}/N and the dimensionless excess chemical potential $\bar{\mu}^{\text{ex}}$ are obtained as $\bar{F}^{\text{ex}}/N = \bar{F}_1/N - \bar{F}_0/N$ and $\bar{\mu}^{\text{ex}} = \bar{\mu}_1 - \bar{\mu}_0$, respectively.

B. Truncation based on the Kirkwood superposition approximation

To implement numerical calculations, the hierarchy of equations must be truncated at a finite order. When truncating the hierarchy at order n , the $(n+1)$ th and $(n+2)$ th order distribution functions appearing in Eq. (11) must be approximated. In doing so, it is essential to ensure that the following cluster decomposability is preserved:

$$\begin{aligned} & y_\lambda^{(k)}(\mathbf{r}_1, \dots, \mathbf{r}_{k-1}) \\ & \approx y_\lambda^{(l)}(\mathbf{r}_1, \dots, \mathbf{r}_{l-1}) \\ & \times y_\lambda^{(k-l)}(\mathbf{r}_{l+1} - \mathbf{r}_l, \dots, \mathbf{r}_{k-1} - \mathbf{r}_l) \\ & \text{when } |\mathbf{r}_{1,\dots,l-1}| \ll |\mathbf{r}_{l,\dots,k-1}|. \quad (13) \end{aligned}$$

In other words, when a group of l particles is sufficiently far from the remaining $k-l$ particles, the k -body distri-

bution function factorizes into the product of the l -body and $(k-l)$ -body distribution functions. If this property does not hold, some of the spatial integrals appearing in Eqs. (10) and (11) will diverge, as the integrands will not decay to zero at infinity.

The KSA is one such approximation that satisfies the cluster decomposability condition. In this approximation, many-body distribution functions are expressed as products of lower-order distribution functions, which is justified in regimes where many-body correlations are weak, such as in the low-density limit. For example, by neglecting three-body and higher-order correlations, $y_\lambda^{(k)}$ can be approximated as a product of two-body distribution functions as follows:

$$y_\lambda^{(k)}(\mathbf{r}_1, \dots, \mathbf{r}_{k-1}) \approx \prod_{i=1}^{k-1} \prod_{j=i+1}^k y_\lambda^{(2)}(\mathbf{r}_j - \mathbf{r}_i) + O(\rho). \quad (14)$$

Here, $\mathbf{r}_k = \mathbf{0}$.

Since Eq. (14) is guaranteed only in the low-density limit, one might expect that applying the KSA to the flow equation would significantly degrade its accuracy at high densities, just as applying it to the Yvon–Born–Green (YBG) equation is known to cause large errors in the virial coefficients [51]. However, we do not necessarily expect this to be the case. In our approach, the integration over λ incorporates higher-order correlations that become important at high densities, allowing partial inclusion of such correlations even when the right-hand side of the flow equation is approximated by the KSA. Furthermore, unlike the YBG equation, the n th-order equation depends not only on the $(n+1)$ th-order correlation function but also on the $(n+2)$ th-order one, suggesting that higher-order correlations can be more effectively captured. In addition, even when approximations are applied to the cavity distribution functions, the exponential factors in the integrands of the flow equations ensure that one of the key contributions—the excluded-volume effect—is properly taken into account.

In this work, we consider the flow equations up to second order and apply the KSA to $y_\lambda^{(3)}$ and $y_\lambda^{(4)}$. As a

result, Eq. (10) and Eq. (11) for $n = 2$ are approximated

as follows:

$$\partial_\lambda \bar{\psi}_\lambda \approx -\beta K_{T,\lambda} \int d\mathbf{r} \partial_\lambda f_\lambda(\mathbf{r}) y_\lambda^{(2)}(\mathbf{r}) \left(1 + \frac{\rho}{2} \int d\mathbf{r}' \left(g_\lambda^{(2)}(\mathbf{r} + \mathbf{r}') g_\lambda^{(2)}(\mathbf{r}') - 1 \right) \right), \quad (15)$$

$$\begin{aligned} \partial_\lambda \ln y_\lambda^{(2)}(\mathbf{r}_1) \approx & \partial_\lambda \bar{\psi}_\lambda \left(2 + \rho \int d\mathbf{r} \left(g_\lambda^{(2)}(\mathbf{r}_1 - \mathbf{r}) g_\lambda^{(2)}(\mathbf{r}) - 1 \right) \right) + 2\rho \int d\mathbf{r} \partial_\lambda f_\lambda(\mathbf{r}) y_\lambda^{(2)}(\mathbf{r}) g_\lambda^{(2)}(\mathbf{r}_1 - \mathbf{r}) \\ & + \frac{\rho^2}{2} \int d\mathbf{r} \int d\mathbf{r}' \partial_\lambda f_\lambda(\mathbf{r} - \mathbf{r}') y_\lambda^{(2)}(\mathbf{r} - \mathbf{r}') \left(g_\lambda^{(2)}(\mathbf{r}) g_\lambda^{(2)}(\mathbf{r}') g_\lambda^{(2)}(\mathbf{r} - \mathbf{r}_1) g_\lambda^{(2)}(\mathbf{r}' - \mathbf{r}_1) - 1 \right). \end{aligned} \quad (16)$$

Here, we have introduced $f_\lambda(\mathbf{r}) = e^{-\bar{v}_\lambda(\mathbf{r})} - 1$. In the derivation, note that $\mathbf{r}_2 = \mathbf{0}$.

C. Reduction of spatial integrals

1. Legendre expansion

Eqs. (15) and (16) contain double spatial integrals of the following form:

$$I(r_1) = \int d\mathbf{r}_2 \int d\mathbf{r}_3 F_1(\mathbf{r}_1, \mathbf{r}_2) F_2(\mathbf{r}_2, \mathbf{r}_3) F_3(\mathbf{r}_3, \mathbf{r}_1). \quad (17)$$

Here, $F_i(\mathbf{r}, \mathbf{r}')$ ($i = 1, 2, 3$) is assumed to depend only on $r = |\mathbf{r}|$, $r' = |\mathbf{r}'|$, and $\cos\theta = \frac{\mathbf{r} \cdot \mathbf{r}'}{rr'}$; that is, $F_i(\mathbf{r}, \mathbf{r}') = F_i(r, r', \cos\theta)$. Reducing the computational cost of this integral is crucial for the feasibility of numerical implementation. To achieve this, we adopt a method based on Legendre expansion [49]. Using this approach, the spatial integral above can be simplified to the following form of a double integral:

$$\begin{aligned} I(r_1) = & \sum_{l=0}^{\infty} \frac{16\pi^2}{(2l+1)^2} \int_0^\infty dr_2 \int_0^\infty dr_3 r_2^2 r_3^2 \\ & \times \tilde{F}_{1,l}(r_1, r_2) \tilde{F}_{2,l}(r_2, r_3) \tilde{F}_{3,l}(r_3, r_1). \end{aligned} \quad (18)$$

Here, $\tilde{F}_{i,l}(r, r')$ denotes the coefficients of the Legendre polynomial expansion of $F_i(r, r', \cos\theta)$, and is defined us-

ing the Legendre polynomial $P_l(t)$ as follows:

$$\tilde{F}_{i,l}(r, r') = \frac{2l+1}{2} \int_{-1}^1 dt F_i(r, r', t) P_l(t). \quad (19)$$

When applying Eq. (18) to Eq. (16), an infinite sum appears. For practical computation, however, a cutoff is introduced to truncate the series.

2. Choice of the evolution of interaction

Depending on the choice of $\bar{v}_\lambda(r)$, the dimensionality of the integrals can be further reduced. Here, we consider a flow in terms of the interaction range, defined as follows:

$$\bar{v}_\lambda(r) = \bar{v}(r)\theta(\lambda r_{\text{cut}} - r). \quad (20)$$

Here, we assume that the interaction is short-ranged, and that there exists a cutoff r_{cut} beyond which the interaction becomes negligibly small. Under Eq. (20), $\partial_\lambda f_\lambda(r)$ appearing in the flow equations can be expressed in terms of a delta function as follows:

$$\partial_\lambda f_\lambda(r) = r_{\text{cut}} f(\lambda r_{\text{cut}}) \delta(\lambda r_{\text{cut}} - r). \quad (21)$$

This appears within the integrand of the flow equations and, as a result, reduces the dimensionality of the integrals. The flow equations after applying Eqs. (18) and (20) take the following form:

$$\partial_\lambda \frac{\bar{F}_\lambda}{N} = -2\pi\lambda^2 \rho r_{\text{cut}}^3 f(\lambda r_{\text{cut}}) y_\lambda^{(2)}(\lambda r_{\text{cut}}), \quad (22)$$

$$\partial_\lambda \bar{\psi}_\lambda \approx 2 \frac{\partial_\lambda \bar{F}_\lambda}{N} \left(1 + 2\pi\beta K_{T,\lambda} \int_0^\infty dr r^2 \tilde{h}_{\lambda,0}(\lambda r_{\text{cut}}, r) h_\lambda^{(2)}(r) \right), \quad (23)$$

$$\begin{aligned} \partial_\lambda \ln y_\lambda^{(2)}(r_1) \approx & -4 \frac{\partial_\lambda \bar{F}_\lambda}{N} \left(\tilde{h}_0(\lambda r_{\text{cut}}, r_1) + 2\pi\rho \int_0^\infty dr' r'^2 \tilde{h}_{\lambda,0}(\lambda r_{\text{cut}}, r') \tilde{h}_{\lambda,0}(r', r_1) (1 + 2h_\lambda(r')) \right. \\ & \left. - 2\pi\beta K_{T,\lambda} \int_0^\infty dr r^2 \tilde{h}_{\lambda,0}(\lambda r_{\text{cut}}, r) h_\lambda^{(2)}(r) \times 2\pi\rho \int_0^\infty dr' r'^2 h_\lambda(r') \tilde{h}_0(r', r_1) \right) \\ & + 8\pi^2 \rho^2 \sum_{l=0}^{\infty} \frac{1}{(2l+1)^2} \int_0^\infty dr \int_0^\infty dr' r^2 r'^2 h_\lambda^{(2)}(r) \tilde{h}_{\lambda,l}(r, r_1) \tilde{Y}_{\lambda,l}(r, r') h_\lambda^{(2)}(r') \tilde{h}_{\lambda,l}(r', r_1), \end{aligned} \quad (24)$$

where $h_\lambda(r) = g_\lambda^{(2)}(r) - 1$ is the total correlation function, $\tilde{h}_{\lambda,l}(r, r')$ is the coefficient of the Legendre polynomial expansion of $h_\lambda(|\mathbf{r} - \mathbf{r}'|)$, and $\tilde{Y}_{\lambda,l}(r, r')$ is the coefficient of the Legendre polynomial expansion of $Y_\lambda(\mathbf{r} - \mathbf{r}') = \partial_\lambda f_\lambda(\mathbf{r} - \mathbf{r}') y_\lambda(\mathbf{r} - \mathbf{r}')$, given by

$$\begin{aligned} \tilde{Y}_{\lambda,l}(r, r') = & \frac{2l+1}{2rr'} \lambda r_{\text{cut}}^2 f(\lambda r_{\text{cut}}) y_\lambda^{(2)}(\lambda r_{\text{cut}}) \\ & \times P_l\left(\frac{r^2 + r'^2 - \lambda^2 r_{\text{cut}}^2}{2rr'}\right) \\ & \times \theta(r + r' - \lambda r_{\text{cut}}) \theta(\lambda r_{\text{cut}} - |r - r'|). \end{aligned} \quad (25)$$

Equations (22)-(24) represent the final forms used in our numerical calculations.

We now discuss the impact on accuracy when using Eq. (20). Without introducing approximations, the results would be independent of the specific choice of the λ -evolution of $\bar{v}_\lambda(r)$; however, the introduction of the KSA introduces such dependence. In the case of incorporating hard-core repulsion, the use of Eq. (20) ensures accuracy in the initial stage of the flow. This is because the dimensionless parameter reduces to the packing fraction $\eta = \pi \rho (\lambda r_{\text{cut}})^3 / 6$, where λr_{cut} is smaller than the particle diameter for the hard-core system, allowing the λ -evolution to be reinterpreted as a density evolution. Consequently, for small λ , the KSA is guaranteed to hold, and the flow equation becomes accurate.

III. ANALYSIS OF LENNARD-JONES FLUID

Here, we apply our method to the Lennard-Jones (LJ) liquid, one of the standard models used to evaluate the performance of methods for classical liquids. The interaction in the LJ liquid is expressed in terms of the depth ϵ and particle diameter σ as follows:

$$v(r) = 4\epsilon \left(\left(\frac{\sigma}{r}\right)^{12} - \left(\frac{\sigma}{r}\right)^6 \right). \quad (26)$$

Using these two parameters, the state of the system is specified by the dimensionless density $\rho^* = \rho \sigma^3$ and the dimensionless temperature $T^* = 1/(\beta\epsilon)$. One of the notable properties of the LJ model is that it exhibits a critical point associated with the liquid–gas phase transition. The critical point is located at $(\rho_c^*, T_c^*) = (\rho_c^*, T_c^*) \approx (0.3, 1.3)$ [1], and for $T^* < T_c^*$, the system undergoes a first-order phase transition as ρ^* increases.

In particular, we address the following two points:

1. For $T^* > T_c^*$, where calculations can be stably performed over a wide range of ρ^* , we compare our results with those of MD and the integral equation methods to assess the accuracy and the thermodynamic consistency of our approach.
2. Near $T = T_c^*$, we examine whether our method is capable of capturing the phase transition.

Details of the numerical setup for FRG are presented in Appendix A, while the MD and integral equation calculations are described in Appendix B.

A. Results for $T^* > T_c^*$

Here, we present the results for thermodynamic quantities and the pair distribution function at $T^* = 1.4 > T_c^*$. We also compare these results with those obtained from MD and integral equation methods. For the integral equation approaches, we employ the hypernetted chain (HNC) [5, 6], Percus–Yevick (PY) [4], and Kovalevko–Hirata (KH) [52] closures.

In addition to accuracy, we examine thermodynamic consistency—that is, the agreement between results obtained from different methods of calculating thermodynamic quantities. To this end, we compute the excess free energy $\bar{F}^{\text{ex}}/N = \bar{F}_1/N - \bar{F}_0/N$, the excess chemical potential $\bar{\psi}^{\text{ex}} = \bar{\psi}_1 - \bar{\psi}_0$, and the pressure P using the following three different methods and compare the discrepancies among them:

1. Calculation using Eqs. (22) and (23).
2. (Virial route) Calculation based on the pair distribution function $g^{(2)}(r) = g_1^{(2)}(r)$ through the pressure equation

$$\beta P = \rho - \frac{2\pi\rho^2}{3} \int_0^\infty dr r^3 \frac{d\bar{v}(r)}{dr} g^{(2)}(r). \quad (27)$$

3. (Compressibility route) Calculation based on $g^{(2)}(r)$ through the density integral of the bulk modulus (inverse compressibility),

$$\beta P = \int_0^\rho d\rho' \frac{\beta K_{T,1}|_{\rho=\rho'}}{\rho'}, \quad (28)$$

together with Eq. (12).

In the first method, P is determined from the obtained \bar{F}^{ex}/N and $\bar{\psi}^{\text{ex}}$ using

$$\beta P = \rho \left(1 + \bar{\psi}^{\text{ex}} - \frac{\bar{F}^{\text{ex}}}{N} \right). \quad (29)$$

In the second and third methods, \bar{F}^{ex}/N and $\bar{\psi}^{\text{ex}}$ are obtained from the resulting P using Eq. (29) and the relation

$$\frac{\bar{F}^{\text{ex}}}{N} = \int_0^\rho d\rho' \frac{1}{\rho'} \left(\frac{\beta P|_{\rho=\rho'}}{\rho'} - 1 \right). \quad (30)$$

For comparison, we also perform calculations using the integral equation methods via both the virial and compressibility routes. For MD simulations, we employ the virial route, since in the compressibility route the integrand of Eq. (12) can have a long tail, leading to significant finite-size effects.

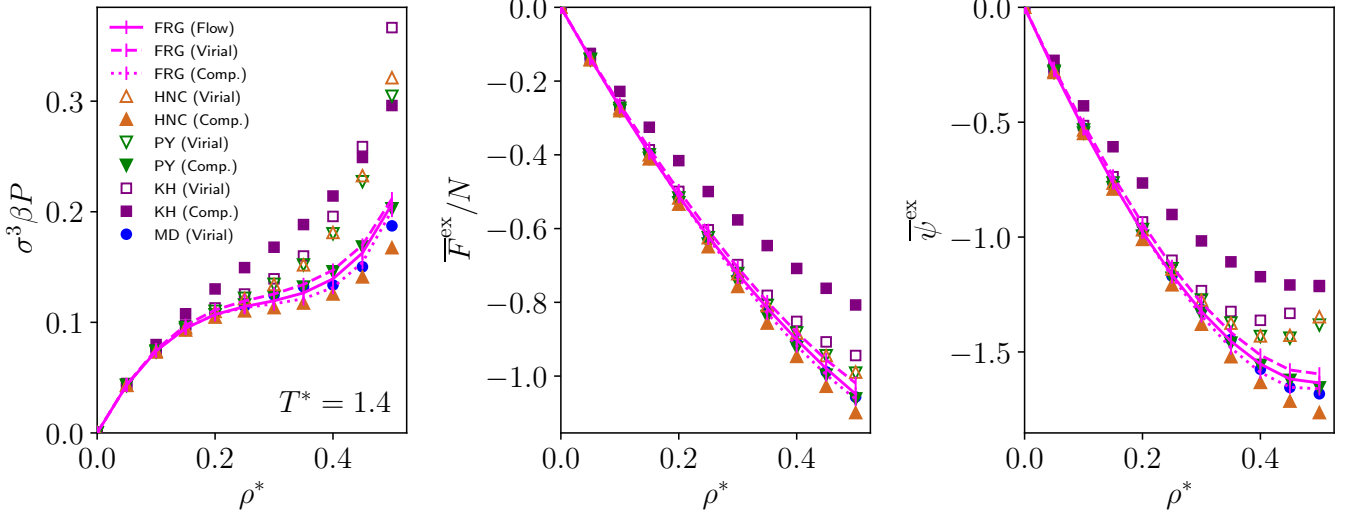


FIG. 1. Density dependence of the pressure P , excess free energy \bar{F}^{ex}/N , and excess chemical potential $\bar{\psi}^{\text{ex}}$ at $T^* = 1.4$. For both the FRG and the integral equation methods (HNC, PY, and KH), results obtained via the virial and compressibility routes are presented and labeled as (Virial) and (Comp.), respectively. In addition, for the FRG, the results obtained using Eqs. (22) and (23) are also shown and labeled as (Flow). The MD results are obtained via the virial route.

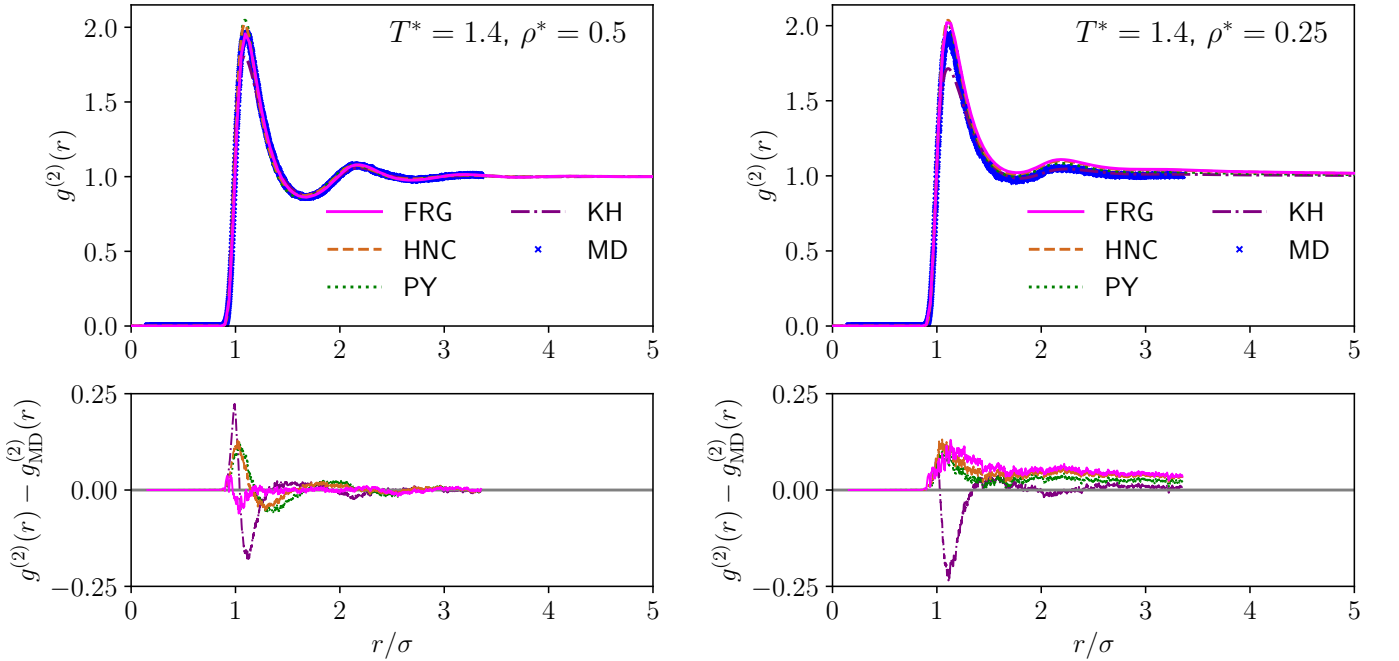


FIG. 2. Pair distribution function results from FRG, integral equation methods (HNC, PY, KH), and MD at $T^* = 1.4$, $\rho^* = 0.5$. The lower panel shows the differences between the MD result $g^{(2)}_{\text{MD}}(r)$ and those of the other methods.

Figure 1 shows the results for P , \bar{F}^{ex}/N , and $\bar{\psi}^{\text{ex}}$. Since this region is close to the critical point, the slope of P with respect to density becomes gentle around $\rho^* = 0.3$. In terms of accuracy, all methods yield results close to those of MD in the low-density region. However, as the density increases, the results obtained from the virial

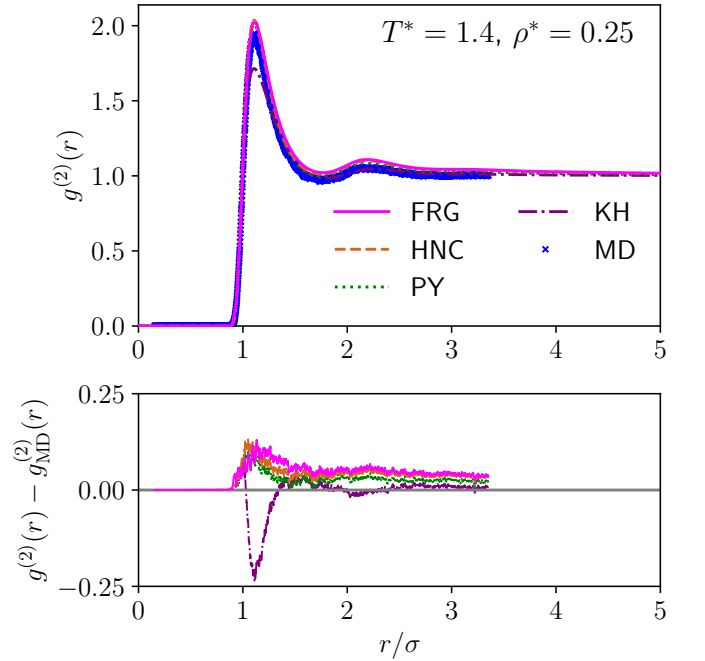


FIG. 3. Same as Fig. 2, but for $\rho^* = 0.25$.

and compressibility routes in the integral equation methods deviate significantly from each other, indicating a severe loss of thermodynamic consistency due to insufficient inclusion of many-body effects. In contrast, the FRG results show much smaller discrepancies between the different routes. Moreover, compared with the integral equation methods, the FRG results reproduce the MD data more accurately for all thermodynamic quantities. These findings suggest that incorporating many-

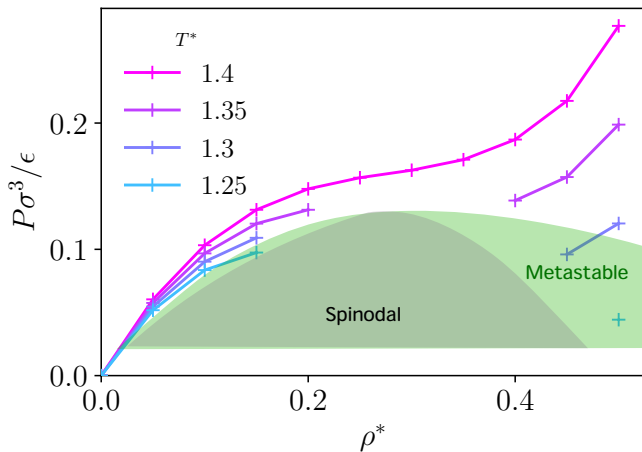


FIG. 4. Density dependence of the pressure obtained from FRG. The gray (green) shaded region indicates the spinodal (metastable) region as suggested by the results.

body effects through the flow equations is highly effective.

Figure 2 shows the pair distribution function $g^{(2)}(r)$ at $\rho^* = 0.5$. Notably, the flow equation method reproduces the MD result for the peak height near $r/\sigma = 1$ more accurately than the integral equation methods. This difference is more clearly visible in the deviations from MD, $g^{(2)}(r) - g_{\text{MD}}^{(2)}(r)$, also shown in the figure. As seen in the results at $\rho^* = 0.25$ in Fig. 3, even at lower densities, the flow equation method reproduces the MD results with accuracy comparable to, or better than, that of the integral equation methods.

B. Results near $T^* = T_c^*$

We examine how the pressure obtained from the flow equation behaves as the temperature T^* crosses the critical temperature $T^* = T_c^*$. Figure 4 shows the change in the density dependence of the pressure near $T^* = T_c^* \approx 1.3$. As the system approaches the critical point, the pressure curve becomes flatter. This behavior indicates that the bulk modulus approaches zero, suggesting the emergence of a region where the integral in Eq. (12) diverges, leading to numerical instability. In fact, we find that such breakdowns start to appear around $T^* \sim 1.35$. In the figure, only the data points for which the calculation remained stable are plotted.

For $T^* < 1.35$, the presence of a gas-liquid first-order phase transition implies the coexistence of low-density (gas) and high-density (liquid) states with the same temperature and pressure. Indeed, our calculations suggest the existence of a region where the pressure decreases with increasing density. This behavior, similar to that obtained in mean-field analyses [1], indicates the presence of metastable homogeneous states. In the figure, the approximate location of the metastable region is shown. The density dependence of the pressure observed in this

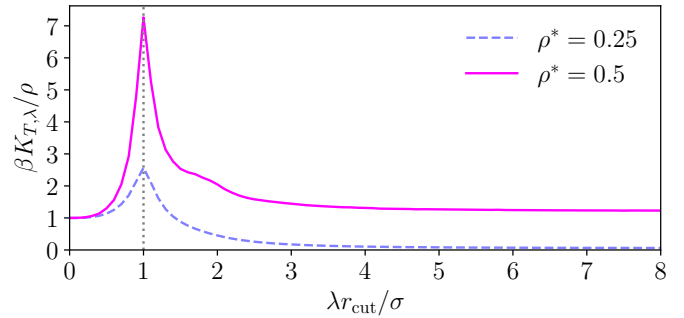


FIG. 5. λ -dependence of the modulus at $T^* = 1.4$ and $\rho^* = 0.25, 0.5$.

region is a characteristic feature of approximate calculations; as the accuracy of the approximation improves and the convexity of the free energy is restored, the pressure curve should become flat. The region where the bulk modulus reaches zero during the flow, leading to numerical breakdown, expands as the temperature decreases. This behavior suggests that uniform-density states become unstable, which can be interpreted as the emergence of a spinodal region.

C. Calculation for higher-density regime

So far, we have presented calculations for $\rho^* \leq 0.5$. At higher densities, however, we encounter numerical breakdown. This can be understood from the evolution of the bulk modulus $K_{T,\lambda}$. Figure 5 shows the results for $K_{T,\lambda}$ at $T^* = 1.4$ and $\rho^* = 0.25, 0.5$. As can be seen from the choice of $\bar{v}_\lambda(r)$ in Eq. (20), the short-range repulsive part of the LJ potential is incorporated when $\lambda r_{\text{cut}}/\sigma < 1$. Consequently, $K_{T,\lambda}$ increases in this regime, and the increase becomes more pronounced at higher densities. At still larger densities, $K_{T,\lambda}$ grows even more rapidly, which, as is evident from Eqs. (23) and (24), leads to a divergence of the flow.

This issue is expected to be avoidable by modifying the choice of flow. In the flow defined by Eq. (20), only the repulsive part is incorporated in the early stage of the evolution. By altering this so that the attractive part is also included to some extent, the rapid increase of $K_{T,\lambda}$ can be prevented. Calculations for the high-density regime based on this idea will be presented in a separate paper.

IV. CONCLUSION

In this paper, we presented a method for analyzing three-dimensional liquids using the functional renormalization group without relying on prior knowledge of a hard-core reference system. As a concrete demonstration, we calculated thermodynamic quantities and the pair distribution function of the Lennard-Jones liquid near its

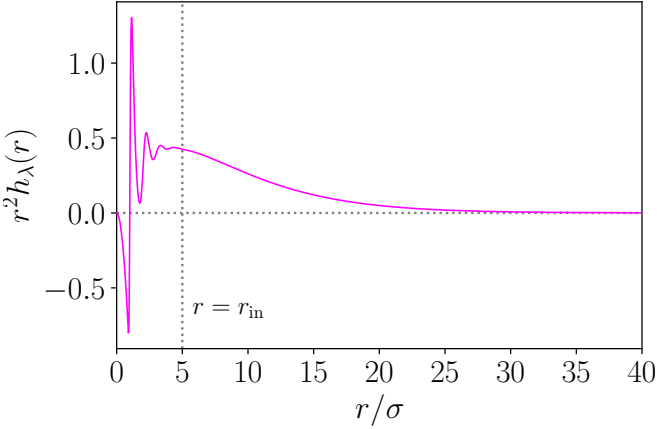


FIG. 6. $r^2 h_\lambda(r)$ at $(\rho^*, T^*) = (0.25, 1.4)$ and $\lambda r_{\text{cut}}/\sigma = 8$.

critical point. We found that our method preserves thermodynamic consistency much more effectively than the integral equation methods and tends to reproduce molecular dynamics results with higher accuracy. Furthermore, near the critical point obtained from molecular dynamics and related studies, the pressure derived from functional renormalization group exhibited softening, successfully capturing the presence of both the critical point and the first-order phase transition.

In this study, we focused on the analysis near the critical point and did not perform calculations in the higher-density regime closer to realistic conditions. As discussed above, we expect that such calculations will become feasible in the future by modifying the choice of interaction evolution. Once a method applicable over a broader density range is established, we aim to extend our approach to realistic solvent systems such as water, with the prospect of contributing to practical chemical calculations.

Further improving computational accuracy within the present framework is another direction for future work. For example, instead of using the KSA, it remains to be investigated whether third- and fourth-order correlations can be determined directly from the flow equations. Another possibility is to incorporate known correction terms to the KSA [53] to enhance accuracy.

ACKNOWLEDGMENTS

T. Y. was supported by JSPS KAKENHI Grant Nos. 25H00177 and 25K23364.

Appendix A: Details of numerical calculation

Here we describe the details of the numerical solution of Eqs. (22)–(24).

To treat $y_\lambda^{(2)}(r)$, we discretize r as follows. In the relatively small range $0 \leq r < r_{\text{in}} = 5\sigma$, where $y_\lambda^{(2)}(r)$ varies

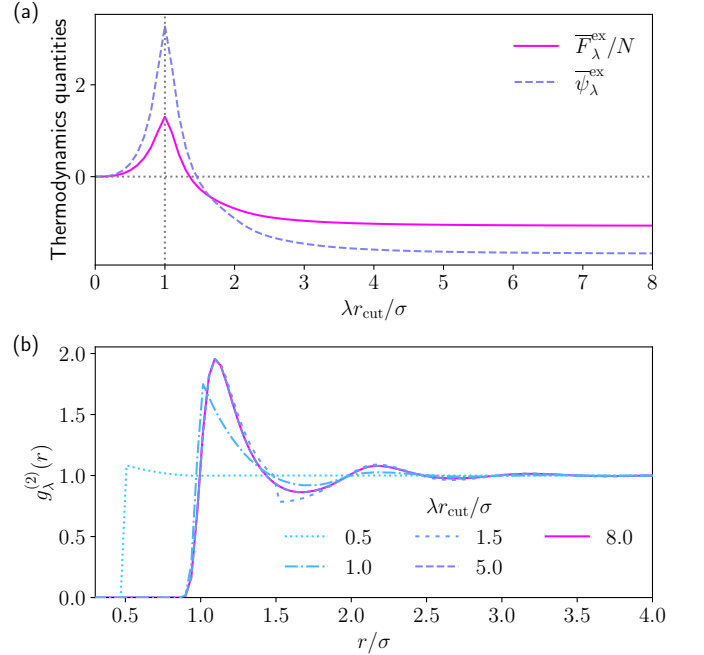


FIG. 7. λ -dependence of $\overline{F}_\lambda^{\text{ex}}/N$, $\overline{\psi}_\lambda^{\text{ex}}$, and $g_\lambda^{(2)}(r)$ in FRG, obtained for $(\rho^*, T^*) = (0.5, 1.4)$.

significantly, we take an equally spaced grid of $N_{\text{in}} = 128$ points, with grid points $r(n)$ ($n = 0, \dots, N_{\text{in}} - 1$) defined by

$$r(n) = \frac{r_{\text{in}}}{N_{\text{in}}} n. \quad (\text{A1})$$

To handle larger values of r without introducing too many grid points, we employ a non-uniform grid in the range $r_{\text{in}} \leq r < r_{\text{out}} = 100\sigma$, where the grid spacing increases at larger r values, reflecting the weaker variation of $y_\lambda^{(2)}(r)$ in that region. Specifically, we take $N_{\text{out}} = 64$ grid points $r(n)$ ($n = N_{\text{in}}, \dots, N_{\text{in}} + N_{\text{out}} - 1$) defined by

$$r(n) = \frac{1}{N_{\text{out}}^2} \left(r_{\text{out}} - \frac{r_{\text{in}} N_{\text{out}}}{N_{\text{in}}} - r_{\text{in}} \right) (n - N_{\text{in}})^2 + \frac{r_{\text{in}}}{N_{\text{in}}} (n - N_{\text{in}}) + r_{\text{in}}. \quad (\text{A2})$$

This construction ensures continuity with Eq. (A1) at $n = N_{\text{in}}$, satisfying both the positional continuity $r(N_{\text{in}}) = r_{\text{in}}$ and the grid-spacing continuity $r'(N_{\text{in}}) = r_{\text{in}}/N_{\text{in}}$, while also fulfilling $r(N_{\text{out}}) = r_{\text{out}}$ and covering the region $[r_{\text{in}}, r_{\text{out}}]$. Handling such a wide range of r is important near the critical point for evaluating $K_{T,\lambda}$, which appears in the flow equations and is expressed from Eq. (12) as

$$K_{T,\lambda} = \frac{\rho}{\beta} \left(1 + 4\pi\rho \int_0^\infty dr r^2 h_\lambda(r) \right)^{-1}. \quad (\text{A3})$$

In fact, as shown in Fig. 6, the integrand $r^2 h_\lambda(r) = r^2 [e^{-\bar{v}_\lambda(r)} y_\lambda^{(2)}(r) - 1]$ can exhibit a long tail extending beyond $r = r_{\text{in}}$.

When evaluating the integrals in Eqs. (23), (24), and (A3), which are computed numerically using Gaussian quadrature, the values of $y_\lambda^{(2)}(r)$ at points other than the grid are required. For $0 \leq r \leq r(N_{\text{in}} + N_{\text{out}} - 1)$, we use values obtained by linear interpolation between grid points, while for larger r we set $y_\lambda^{(2)}(r) = 1$.

For the cutoff r_{cut} appearing in Eq. (20), we set $r_{\text{cut}} = 5\sigma$. Figure 7 shows the evolution of $\bar{F}_\lambda^{\text{ex}}/N$, $\bar{\psi}_\lambda^{\text{ex}}$, and $g_\lambda^{(2)}(r)$ obtained by solving the flow equations. With $r_{\text{cut}} = 8\sigma$, these quantities are seen to converge at $\lambda = 1$.

The remaining numerical details are as follows. For the infinite sum over l in Eq. (24), we introduce a cutoff $L_{\text{max}} = 10$ and confirm the convergence of the results. To solve the λ -evolution of Eqs. (22)-(24), we employ an eighth-order Runge–Kutta method. The implementations of Gaussian quadrature, linear interpolation of $y_\lambda^{(2)}(r(n))$, and the Runge–Kutta method are carried out using the Gnu Scientific Library [54]. Furthermore, we accelerate the computations by parallelizing the evaluation of Eq. (24) at different grid points $r_1 = r(n)$ with OpenMP.

Appendix B: Molecular dynamics and integral equation methods

Here, we summarize the setup of the MD calculations and the integral equation methods used in this paper.

1. Molecular dynamics

For the MD simulations, we use the PIMD package [55]. We simulate 256 argon atoms in a cubic box with periodic boundary conditions, choosing the box length to reproduce the target density. The time evolution is

carried out up to 0.25 ns with a time step of 0.5 fs, corresponding to 5×10^5 steps. A massive Nosé–Hoover thermostat chain is employed to control the temperature.

2. Integral equation method

The integral equation method is based on the following Ornstein–Zernike equation [3]:

$$\tilde{c}(|\mathbf{k}|) = \frac{\tilde{h}(|\mathbf{k}|)}{1 + \rho \tilde{h}(|\mathbf{k}|)}, \quad (\text{B1})$$

where $\tilde{c}(|\mathbf{k}|)$ and $\tilde{h}(|\mathbf{k}|)$ are the three-dimensional Fourier transforms of the direct correlation function $c(|\mathbf{r}|)$ and the total correlation function $h(|\mathbf{r}|) = g^{(2)}(|\mathbf{r}|) - 1$, respectively. In the integral equation method, an approximate relation, called a closure, is introduced to solve the Ornstein–Zernike equation. In this work, we employ the following three closures:

1. Hypernetted chain (HNC) [5, 6]:

$$g^{(2)}(r) \approx e^{-\bar{v}(r)+h(r)-c(r)}.$$

2. Percus–Yevick equation (PY) [4]:

$$g^{(2)}(r) \approx e^{-\bar{v}(r)} (1 + h(r) - c(r)).$$

3. Kovalenko–Hirata closure (KH) [52]:

$$g^{(2)}(r) \approx e^{d(r)} \theta(-d(r)) + (1 + d(r)) \theta(d(r)),$$

$$\text{with } d(r) = -\bar{v}(r) + h(r) - c(r).$$

In the numerical calculations, we used a grid of 6851 points for r over the range $0 \leq r \leq 50\sigma$. The solutions were obtained using an iterative method.

[1] J. Hansen and I. McDonald, *Theory of Simple Liquids: with Applications to Soft Matter* (Elsevier Science, 2013).

[2] S. Nishihara and M. Otani, Hybrid solvation models for bulk, interface, and membrane: Reference interaction site methods coupled with density functional theory, *Phys. Rev. B* **96**, 115429 (2017).

[3] L. Ornstein and F. Zernike, Accidental deviations of density and opalescence at the critical point of a single substance, *Koninklijke Nederlandse Akademie van Wetenschappen Proceedings Series B Physical Sciences* **17**, 793 (1914).

[4] J. K. Percus and G. J. Yevick, Analysis of classical statistical mechanics by means of collective coordinates, *Phys. Rev.* **110**, 1 (1958).

[5] T. Morita and K. Hiroike, A new approach to the theory of classical fluids. I, *Progress of Theoretical Physics* **23**, 1003 (1960).

[6] R. J. Baxter, Ornstein–Zernike relation for a disordered fluid, *Australian Journal of Physics* **21**, 563 (1968).

[7] Y. Rosenfeld and N. W. Ashcroft, Theory of simple classical fluids: Universality in the short-range structure, *Phys. Rev. A* **20**, 1208 (1979).

[8] F. J. Rogers and D. A. Young, New, thermodynamically consistent, integral equation for simple fluids, *Phys. Rev. A* **30**, 999 (1984).

[9] C. Ebner, W. F. Saam, and D. Stroud, Density-functional theory of simple classical fluids. i. surfaces, *Phys. Rev. A* **14**, 2264 (1976).

[10] A. J. M. Yang, P. D. Fleming, and J. H. Gibbs, Molecular theory of surface tension, *J. Chem. Phys.* **64**, 3732 (1976).

[11] W. F. Saam and C. Ebner, Density-functional theory of classical systems, *Phys. Rev. A* **15**, 2566 (1977).

[12] R. Evans, The nature of the liquid-vapour interface and other topics in the statistical mechanics of non-uniform, classical fluids, *Advances in Physics* **28**, 143 (1979).

[13] Y. Rosenfeld, Free-energy model for the inhomogeneous

hard-sphere fluid mixture and density-functional theory of freezing, *Phys. Rev. Lett.* **63**, 980 (1989).

[14] Y. Rosenfeld, D. Levesque, and J. Weis, Free-energy model for the inhomogeneous hard-sphere fluid mixture: Triplet and higher-order direct correlation functions in dense fluids, **92**, 6818.

[15] Y. Rosenfeld, Free-energy model for the inhomogeneous hard-sphere fluid: “closure” relation between generating functionals for “direct” and “cavity” distribution functions, **93**, 4305.

[16] Y. Rosenfeld, Free-energy model for the inhomogeneous hard-sphere fluid in d dimensions: Structure factors for the hard-disk ($d=2$) mixtures in simple explicit form, *Phys. Rev. A* **42**, 5978 (1990).

[17] Y. Tang and J. Wu, A density-functional theory for bulk and inhomogeneous lennard-jones fluids from the energy route, **119**, 7388.

[18] A. Parola and L. Reatto, Hierarchical reference theory of fluids and the critical point, *Phys. Rev. A* **31**, 3309 (1985).

[19] L. W. Salvino and J. A. White, Calculation of density fluctuation contributions to thermodynamic properties of simple fluids, *The Journal of Chemical Physics* **96**, 4559 (1992).

[20] A. Parola, D. Pini, and L. Reatto, First-order phase transitions, the maxwell construction, and the momentum-space renormalization group, *Phys. Rev. E* **48**, 3321 (1993).

[21] J. A. White and S. Zhang, Renormalization group theory for fluids, *The Journal of Chemical Physics* **99**, 2012 (1993).

[22] A. Parola and L. Reatto, Liquid state theories and critical phenomena, *Advances in Physics* **44**, 211 (1995).

[23] J. A. White and S. Zhang, Renormalization theory of nonuniversal thermal properties of fluids, *The Journal of Chemical Physics* **103**, 1922 (1995).

[24] J.-M. Caillol, Non-perturbative renormalization group for simple fluids, *Molecular Physics* **104**, 1931 (2006).

[25] A. Parola, D. Pini, and L. Reatto, Liquid-vapor transition from a microscopic theory: Beyond the maxwell construction, *Phys. Rev. Lett.* **100**, 165704 (2008).

[26] A. Parola, D. Pini, and L. Reatto, The smooth cut-off hierarchical reference theory of fluids, *Molecular Physics* **107**, 503 (2009).

[27] J.-M. Caillol, Link between the hierarchical reference theory of liquids and a new version of the non-perturbative renormalization group in statistical field theory, *Molecular Physics* **109**, 2813 (2011).

[28] A. Parola and L. Reatto, Recent developments of the hierarchical reference theory of fluids and its relation to the renormalization group, *Molecular Physics* **110**, 2859 (2012).

[29] L. Lue, Application of the functional renormalization group method to classical free energy models, *AIChE Journal* **61**, 2985.

[30] S. Iso and K. Kawana, Density Renormalization Group for Classical Liquids, *Prog. Theor. Exp. Phys.* **2019**, 013A01 (2019), arXiv:1808.08133 [cond-mat.stat-mech].

[31] T. Yokota, J. Haruyama, and O. Sugino, Functional-renormalization-group approach to classical liquids with short-range repulsion: A scheme without repulsive reference system, *Phys. Rev. E* **104**, 014124 (2021).

[32] F. J. Wegner and A. Houghton, Renormalization Group Equation for Critical Phenomena, *Phys. Rev. A* **8**, 401 (1973).

[33] K. G. Wilson and J. Kogut, The renormalization group and the ϵ expansion, *Phys. Rep.* **12**, 75 (1974).

[34] J. Polchinski, Renormalization and effective lagrangians, *Nucl. Phys. B* **231**, 269 (1984).

[35] C. Wetterich, Exact evolution equation for the effective potential, *Phys. Lett. B* **301**, 90 (1993).

[36] J. Polonyi and K. Sailer, Effective actions and the density functional theory, *Phys. Rev. B* **66**, 155113 (2002).

[37] A. Schwenk and J. Polonyi, Towards density functional calculations from nuclear forces, in *32nd International Workshop on Gross Properties of Nuclei and Nuclear Excitation: Probing Nuclei and Nucleons with Electrons and Photons (Hirschegg 2004)* Hirschegg, Austria, January 11-17, 2004 (2004) pp. 273–282, arXiv:nucl-th/0403011.

[38] S. Kemler and J. Braun, Towards a renormalization group approach to density functional theory—general formalism and case studies, *J. Phys. G* **40**, 085105 (2013).

[39] J. F. Rentrop, S. G. Jakobs, and V. Meden, Two-particle irreducible functional renormalization group schemes—a comparative study, **48**, 145002 (2015).

[40] S. Kemler, M. Pospiech, and J. Braun, Formation of selfbound states in a one-dimensional nuclear model—a renormalization group based density functional study, *J. Phys. G* **44**, 015101 (2017).

[41] H. Liang, Y. Niu, and T. Hatsuda, Functional renormalization group and Kohn-Sham scheme in density functional theory, *Phys. Lett. B* **779**, 436 (2018).

[42] T. Yokota, K. Yoshida, and T. Kunihiro, Functional renormalization-group calculation of the equation of state of one-dimensional uniform matter inspired by the Hohenberg–Kohn theorem, *Phys. Rev. C* **99**, 024302 (2019).

[43] T. Yokota, K. Yoshida, and T. Kunihiro, *Ab initio* description of excited states of 1D uniform matter with the Hohenberg–Kohn-theorem-inspired functional-renormalization-group method, *Prog. Theor. Exp. Phys.* **2019**, 011D01 (2019).

[44] T. Yokota and T. Naito, Functional-renormalization-group aided density functional analysis for the correlation energy of the two-dimensional homogeneous electron gas, *Phys. Rev. B* **99**, 115106 (2019).

[45] T. Yokota, H. Kasuya, K. Yoshida, and T. Kunihiro, Microscopic derivation of density functional theory for superfluid systems based on effective action formalism, *Prog. Theor. Exp. Phys.* **2021**, 013A03 (2020).

[46] T. Yokota and T. Naito, Ab initio construction of the energy density functional for electron systems with the functional-renormalization-group-aided density functional theory, *Phys. Rev. Research* **3**, L012015 (2021).

[47] T. Yokota and T. Naito, Construction of energy density functional for arbitrary spin polarization using functional renormalization group, *Phys. Rev. B* **105**, 035105 (2022).

[48] J. G. Kirkwood, Statistical mechanics of fluid mixtures, *The Journal of Chemical Physics* **3**, 300 (1935).

[49] J. A. Barker and J. J. Monaghan, Fourth virial coefficients for the 12–6 potential, **36**, 2564.

[50] N. Dupuis, L. Canet, A. Eichhorn, W. Metzner, J. Pawłowski, M. Tissier, and N. Wschebor, The nonperturbative functional renormalization group and its applications, *Physics Reports* **910**, 1 (2021).

[51] V. D. GROUBA, A. V. ZORIN, and L. A. SEVASTIANOV, The superposition approximation: A critical review, *International Journal of Modern Physics B* **18**, 1

(2004).

[52] A. Kovalenko and F. Hirata, Self-consistent description of a metal–water interface by the kohn–sham density functional theory and the three-dimensional reference interaction site model, *The Journal of Chemical Physics* **110**, 10095 (1999).

[53] R. Abe, On the kirkwood superposition approximation, *Progress of Theoretical Physics* **21**, 421 (1959).

[54] M. Galassi, J. Davies, J. Theiler, B. Gough, and G. Jungman, *GNU Scientific Library - Reference Manual, Third Edition, for GSL Version 1.12 (3. ed.)*. (2009).

[55] M. Shiga, PIMD version 2.7.0 (2025).